6

ADATOM STRUCTURES ON SiC(0001) AND Si(111)

We present a study of the adatom structures of SiC(0001) and Si(111) at elevated temperatures. We use Spot-Profile-Analysis Low Energy Electron Diffraction to investigate these surfaces in equilibrium as a function of temperature and external silicon flux. We find that the Si(111)-$'(1\times1)'$ surface is covered with a lattice gas of Si adatoms with constant density over a temperature range of $T = 900\,^{\circ}\mathrm{C}$ to $T = 1150\,^{\circ}\mathrm{C}$. This constant-density lattice gas is in equilibrium with the step edges which act as Si adatom supplies to compensate the loss of evaporating Si adatoms. On the SiC(0001) surface a similar Si adatom structure is formed at high temperature. However, no lattice gas is formed. On the SiC(0001) the Si adatoms arrange in a $(\sqrt{3}\times\sqrt{3})$-layer. The surface area covered by this Si adlayer decreases with increasing temperature since the step edges on the SiC surface cannot supply Si adatoms without also supplying C atoms which leads to the formation of a carbon-rich $(6\sqrt{3}\times6\sqrt{3})$-phase and finally graphene at higher temperature. By investigating the temperature evolution of this decaying $(\sqrt{3}\times\sqrt{3})$-adlayer we found a new additional (1×1)-phase which exists over a small temperature range of a few degrees Celsius below the transition temperature to the $(6\sqrt{3}\times6\sqrt{3})$-phase.

Part of this chapter has been submitted for publication as: S. M. Schramm, J. B. Hannon, S. J. van der Molen, R. M. Tromp, *Adatom structures on SiC*(0001) *and Si*(111).

6.1 INTRODUCTION

Graphene, a single monolayer of carbon in a hexagonal 'honeycomb' arrangement, has attracted considerable interest due to its peculiar electronic properties such as high electronic carrier mobility and ballistic transport up to room-temperature [1] and novel magneto-transport properties [2–4]. Therefore, it has great potential for technological applications such as single-molecule gas sensors [5], in spintronics devices [6–8] or as successor of silicon in the semiconductor device industry [9–11]. All of these applications require uniform high quality graphene on a large scale. One promising route to grow graphene suitable for large-scale production of graphene-based devices is the in-vacuum decomposition of SiC at elevated temperature [9, 12]. Heating SiC in vacuum will cause Si atoms to sublime leaving behind an excess of carbon atoms. These excess carbon atoms self-assemble into graphene. During Si sublimation, the SiC surface changes its structure undergoing a sequence of surface phase transitions [12, 13]. Details of the phase formation sequence and the interface structure between the SiC substrate and the graphene are highly relevant to understand structural quality and electronic properties of the graphene overlayer. Furthermore, it is important to understand the thermodynamics and the kinetics of these phase formations. It has been reported previously that the phase transition temperatures can be shifted by several hundred degrees Celsius by balancing the rate of Si sublimation with an external Si flux, i.e. a Si gas background pressure [13]. At the same time this also leads to a change of the phase transition time scales by several orders of magnitude. Therefore, a dramatic improvement of the morphology of the C-rich phases, including graphene, can be achieved [14].

Now, let us have a more detailed look at the phase formation sequence. Figure 6.1 shows a diagram of the generally accepted phase formation sequence. At low temperature we start with a Si-rich (3×3)-phase. Upon heating, the SiC surface will become increasingly Si-depleted. Therefore, we will observe a phase transition from the (3×3) to the (1×1) structure. Further heating will lead to the $(\sqrt{3} \times \sqrt{3})$-phase where the SiC substrate is covered with 1/3 ML of Si adatoms arranged in a $(\sqrt{3} \times \sqrt{3})$-layer. Additional sublimation of Si from the substrate will yield the carbon-rich $(6\sqrt{3} \times 6\sqrt{3})$-phase which consists of the first graphene-like atomic layer of carbon on top of the SiC substrate. During prolonged heating additional layers of graphene will be formed.

Here, we will investigate the structural transition between the last Si-decorated surface structure, the $(\sqrt{3} \times \sqrt{3})$-phase, to the first carbon layer, the C-rich $(6\sqrt{3} \times 6\sqrt{3})$-phase. Using temperature dependent Spot-Profile-Analysis Low Energy Electron Diffraction (SPA-LEED) we find for the first time an additional intermediate (1×1)-phase between the previously reported $(\sqrt{3} \times \sqrt{3})$-phase and the $(6\sqrt{3} \times$

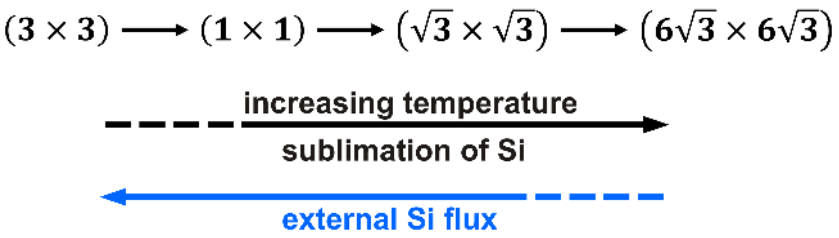

FIGURE 6.1: Diagram of the generally accepted phase formation sequence of the SiC(0001) surface. Starting with a Si-rich phase at low temperature on the right the surface undergoes several phase transitions upon heating until a C-rich phase is reached on the left. Heating the SiC(0001) causes sublimation of Si surface atoms which can be balanced by an external Si flux [13].

$6\sqrt{3}$)-phase. While the transition from the additional (1×1) to the $(6\sqrt{3} \times 6\sqrt{3})$-phase happens over a relatively small temperature interval, the transition from $(\sqrt{3} \times \sqrt{3})$ to the additional (1×1) stretches over ~ 30 degrees Celsius. The coverage and average domain size of the $(\sqrt{3} \times \sqrt{3})$ phase decreases upon heating until the surface is covered by only a pure (1×1)-phase.

Similar to the SiC(0001)-$(\sqrt{3} \times \sqrt{3})$-phase a Si adatom structure can be observed on the Si(111) surface at high temperature. The intriguing complexity of the structures and properties of the Si(111) surface has spurred numerous studies. From these previous reports we know that at room temperature the clean equilibrated Si(111) surface is covered with a (7×7) dimer-adatom-stacking fault layer (DAS) [15]. At temperatures higher than about 860 °C a reversible first-order surface phase transition from the (7×7)-DAS to a disordered $'(1 \times 1)'$ phase is observed [16–19]. It is well established that the $'(1 \times 1)'$-phase consists of a relaxed bulklike structure with random Si adatoms [20–24]. These adatoms arrange in a diffuse $(\sqrt{3} \times \sqrt{3})$ structure somewhat similar to the $(\sqrt{3} \times \sqrt{3})$-phase on SiC(0001).

In the present work, we investigate the structure of the Si(111)-$'(1 \times 1)'$-phase as a function of temperature using SPA-LEED. We are able to determine and quantify the Si adatom gas concentration by comparison with calculated LEED spot-profiles obtained from Monte Carlo (MC) type simulations of lattice gas adatom structures. From the same MC simulations we gain insight into the real space structure of the Si adatom layer of the $'(1 \times 1)'$-phase.

6.2 EXPERIMENT

All Low Energy Electron Microscopy (LEEM) and LEED experiments presented here were performed in the IBM LEEM-II instrument [25] at the T.J. Watson Research

Center in Yorktown Heights, USA. The SiC(0001) samples (Cree) were cleaned inside the LEEM system by outgassing at ≈ 800 °C for 24 h. Subsequently, the samples were exposed at this temperature to disilane gas at a pressure of about 1×10^{-7} Torr for several minutes. The sample surface shows a clear and distinct (3×3) LEED pattern after this cleaning routine. Disilane gas is used as an external source of Si atoms. It decomposes thermally at around 640 °C. The Si gas background pressure in the sample chamber is taken as twice the disilane partial pressure since each disilane atom contains two Si atoms. The Si(111) samples were cleaned by outgassing at ≈ 800 °C for 24 h and subsequent repeated flashing to ≈ 1200 °C. After this treatment the samples showed clear and distinct (1×1) (above T_C) and (7×7) (below T_C) LEED pattern. The influence of an external Si flux on the phase transition temperature is only minor in the case of Si(111) as reported by Hannon et al. [26]. Therefore, the experiments on Si(111) were performed in UHV without an external Si flux. Sample temperatures were measured with an IR-pyrometer. The pyrometer is calibrated using known phase transition temperatures of the sample, i.e either SiC(0001) [13] or Si(111) [16–19]. Temperatures are reproducible to within ≈ 30 degrees Celsius.

6.3 RESULTS

First, we will present the results obtained from measurements on the SiC(0001) surface as a function of temperature and external Si flux. Next, we will then discuss the outcome of our experiments on the Si(111) surface as a function of temperature.

6.3.1 SIC(0001)

The growth of high-quality large-scale graphene on the SiC(0001) surface is possible by in-vacuum sublimation of Si atoms. The SiC(0001) surface undergoes a sequence of phase transitions with increasing Si depletion. It has been reported earlier [13] that these phase transitions can be observed in bright-field LEEM due to the fact that each surface structure gives rise to a different image contrast. Let us assume that we start with an equilibrated (3×3) surface. By heating the sample slowly enough such that the surface remains in quasi-equilibrium we will start to see contrast due to the (1×1)-phase in the image. The temperature at which the contrast due to the (1×1) structure starts to appear is taken as the phase transition temperature. Similarly, the phase transition temperature of the $(1 \times 1) - (\sqrt{3} \times \sqrt{3})$ transition is determined by the temperature at which the contrast due to the (1×1) structure appears in the image upon cooling, analogous to the definition in Ref.[13]. The $(\sqrt{3} \times \sqrt{3}) - (6\sqrt{3} \times 6\sqrt{3})$ transition temperature is given by the temperature at which - upon heating - the $(6\sqrt{3} \times 6\sqrt{3})$ shows up as contrast in the

bright-field LEEM image. Using these procedures we recorded the $(3\times3)-(1\times1)$, the $(1\times1)-(\sqrt{3}\times\sqrt{3})$, and the $(\sqrt{3}\times\sqrt{3})-(6\sqrt{3}\times6\sqrt{3})$ phase transition temperatures at different Si pressures in the range between $p=4\times10^{-8}$ Torr and $p=9\times10^{-7}$ Torr. Our data is in very good agreement with the results published by Tromp et al. [13]. Here, the goal is to study the structure and evolution of the $(\sqrt{3}\times\sqrt{3})$-phase in greater detail. The $(\sqrt{3}\times\sqrt{3})$-phase is the last Si decorated surface structure - upon heating - before the transition to the carbon-rich $(6\sqrt{3}\times6\sqrt{3})$-phase.

We recorded the LEED pattern of the in-equilibrium SiC(0001) surface as a function of sample temperature just above the $(1\times1)-(\sqrt{3}\times\sqrt{3})$ phase transition up to the $(\sqrt{3}\times\sqrt{3})-(6\sqrt{3}\times6\sqrt{3})$ phase transition (see Fig. 6.2). Such a temperature-dependent LEED pattern sequence was recorded at five different Si background gas pressures in the range from about 4×10^{-8} Torr to 9×10^{-7} Torr. Figure 6.3a shows temperature-dependent $\sqrt{3}$-spot profiles taken through the center of the $\sqrt{3}$-spots in the corresponding LEED pattern (similar to the ones in Fig. 6.2) at $p_{\mathrm{Si}}=8.8\times10^{-7}$ Torr. We can clearly see that the peak intensity decreases with increasing sample temperature until the spots completely vanish at very high temperatures. The spot profiles can nicely be reproduced by Lorentzian functions of the form $L(x)=\frac{a\omega}{(x-c)^2+\omega^2}$ with amplitude a, width ω, and center position c. By fitting such Lorentzians to the spot profiles such as those in Fig. 6.3a we obtain the full width at half maximum (FWHM) of the $\sqrt{3}$-spot as a function of temperature and Si gas pressure. Figure 6.3b shows the temperature-dependence of the FWHM at five different Si gas pressures. We find that for each temperature sequence there is a range of constant FWHM at low temperature (limited by the k-resolution in the measurement imposed by the detector of ≈ 0.035 nm^{-1}) and at high temperature there is a range where an increase of the FWHM with increasing temperature is observed. The onset of the high temperature broadening of the $\sqrt{3}$-spot is determined by the temperature at which the FWHM starts to increase. The temperature at which the spot-width broadening starts increases exponentially with the Si gas pressure similar to the pressure-dependence of the previously reported phase transition temperatures on SiC(0001) [13].

Figure 6.4 shows the temperature-pressure-phase diagram of the SiC(0001) surface. We measured the Si pressure-dependent phase transition temperatures of the $(1\times1)-(\sqrt{3}\times\sqrt{3})$ transition (green squares) and the $(\sqrt{3}\times\sqrt{3})-(6\sqrt{3}\times6\sqrt{3})$ transition (blue circles). In addition, the temperature at which the broadening of the $\sqrt{3}$-spots starts, T_{B}, is also plotted in Fig. 6.4 as a function of Si pressure (red diamonds). The diagram clearly shows that there is a temperature window of ~ 30 degrees Celsius between the perfect $(\sqrt{3}\times\sqrt{3})$-layer structure and the $(6\sqrt{3}\times6\sqrt{3})$-phase where we observe a broadening and decay of the $\sqrt{3}$-spots (light red area in Fig. 6.4). In this temperature window a coexistence of a decaying $(\sqrt{3}\times\sqrt{3})$-phase and a (1×1)-phase is observed. With increasing temperature, the fraction of the

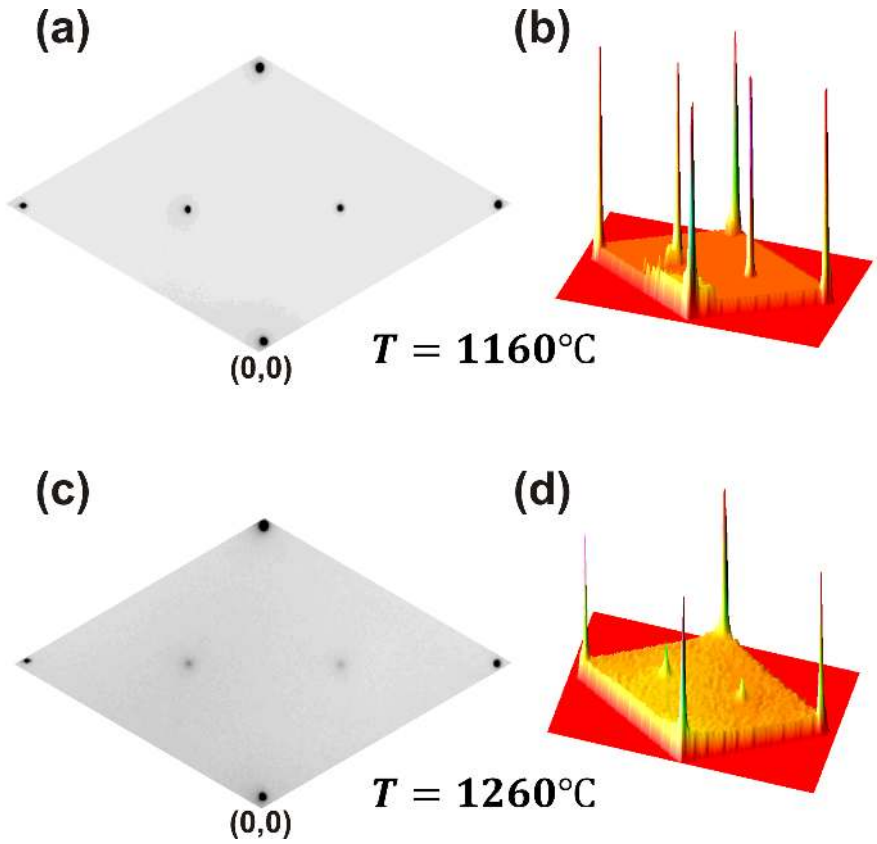

FIGURE 6.2: LEED patterns of the SiC(0001) – $(\sqrt{3}\times\sqrt{3})$ surface at a temperature below the onset of the $\sqrt{3}$-broadening ((a) and (b): $T = 1160\,^{\circ}$C) and above ((c) and (d): $T = 1260\,^{\circ}$C) all at a Si background pressure of 8.8×10^{-7} Torr. (b) and (d) are 3D intensity plots of the patterns in (a) and (c), respectively.

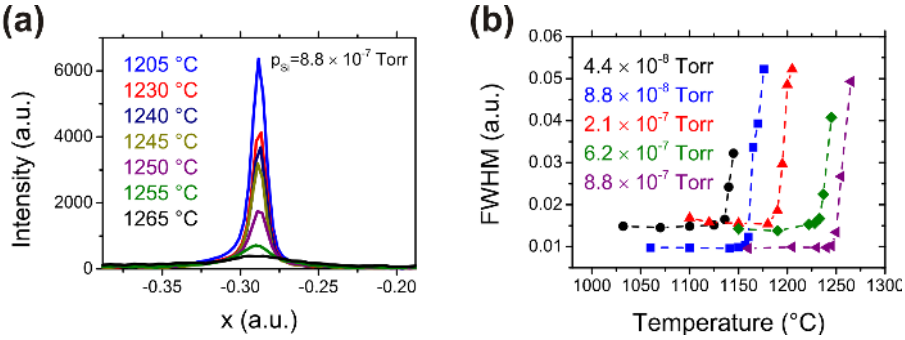

FIGURE 6.3: (a) Profile plots of the $\sqrt{3}$-spots of the SiC(0001) surface as a function of sample temperature at a Si background pressure of 8.8×10^{-7} Torr. (b) FWHM of the $\sqrt{3}$-spot extracted from profile plots such as those in (a) as a function of temperature for different external Si gas pressures.

surface covered with $(\sqrt{3} \times \sqrt{3})$-domains decreases, as Si atoms evaporate from the surface - until equilibrium with the external Si flux is reached - and the $(\sqrt{3} \times \sqrt{3})$-layer breaks up in domains that shrink with increasing temperature, coexisting with a (1×1) structure. Just below the transition temperature to the $(6\sqrt{3} \times 6\sqrt{3})$-phase - in a very narrow temperature window - only a bare (1×1)-phase exists (yellow line in Fig. 6.4) and the $(\sqrt{3} \times \sqrt{3})$-structure has completely vanished. This is the first time that this additional (1×1)-phase has been observed. It is very difficult to detect because it only exists in a very small temperature range. By looking at the temperature-evolution of the $(\sqrt{3} \times \sqrt{3})$-structure, however, we find clear evidence for the existence of such an additional (1×1)-phase before the transition to the first carbon-rich $(6\sqrt{3} \times 6\sqrt{3})$-phase.

The heat of sublimation of the phase transitions indicated in Fig. 6.4 can be estimated by using the Clausius-Clapeyron relation

$$\ln p = -\frac{L}{R}\frac{1}{T} + c \tag{6.1}$$

with p the vapor pressure, T temperature, L the latent heat of sublimation, R the gas constant, and c a constant. Using this relation we find that the heat of sublimation is $L_1 = 3.7 \pm 0.8 \times 10^2$ kJ per mole for the $(1 \times 1) - (\sqrt{3} \times \sqrt{3})$ transition, $L_2 = 4.7 \pm 0.4 \times 10^2$ kJ per mole for the transition from sharp $\sqrt{3}$-spots to broadening spots, and $L_3 = 4.1 \pm 0.6 \times 10^2$ kJ per mole for the $(1 \times 1) - (6\sqrt{3} \times 6\sqrt{3})$ transition. These values are the same within the error and are close to the heat of sublimation of Si from Si $L_{Si} = 4.5 \pm 0.1 \times 10^2$ kJ per mole [13, 27].

The average $(\sqrt{3} \times \sqrt{3})$ domain size is inversely proportional to the FWHM of the corresponding diffraction spots. In Fig. 6.5 we plot this average domain size

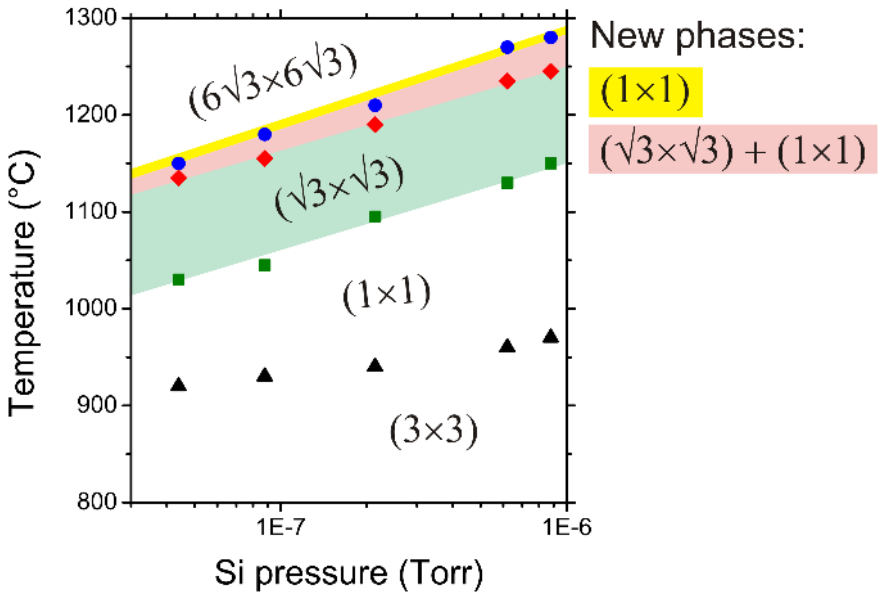

FIGURE 6.4: Temperature-pressure-phase diagram of the SiC(0001) surface. Indicated are the three well known phase transition temperatures of $(3\times3)-(1\times1)$ (black triangles), $(1\times1)-(\sqrt{3}\times\sqrt{3})$ (green squares), and $(\sqrt{3}\times\sqrt{3})-(6\sqrt{3}\times6\sqrt{3})$ (blue circles). In addition the onset temperature of the $\sqrt{3}$-spot broadening is indicated (red diamonds). The green area corresponds to the temperature range where the FWHM of the $\sqrt{3}$-spots is constant. Broadening and decay of the $\sqrt{3}$-spots is observed in the range indicated in red. The yellow line denotes the very small temperature range where an additional (1×1)-phase is observed.

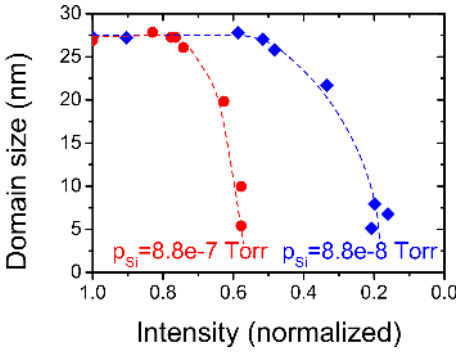

FIGURE 6.5: Average domain size of the $(\sqrt{3}\times\sqrt{3})$-adlayer as a function of integrated $\sqrt{3}$-spot intensity for Si pressures of $p = 8.8e-7$ Torr (red) and $p = 8.8e-8$ Torr (blue).

as a function of the integrated diffraction spot intensity for two different Si pressures, i.e $p = 8.8\times10^{-7}$ Torr (red) and $p = 8.8\times10^{-8}$ Torr (blue). From this plot we conclude that the transition from the $(\sqrt{3}\times\sqrt{3})$ adatom structure to the bulklike (1×1)-phase without any adatoms is induced by a gradual disappearance of the $\sqrt{3}$ phase, accompanied by a reduction of the $\sqrt{3}$ domain size. At the same $\sqrt{3}$ coverage, the average domain size is smaller at higher temperature, presumably due to entropic effects.

6.3.2 Si(111)

As already mentioned in the introduction (section 6.1) the Si(111) surface exhibits a (7×7)-DAS reconstruction at temperatures below $T_C \approx 860\,^{\circ}$C. Above T_C the Si(111) surface shows a $'(1\times1)'$ structure with random adatoms which can be considered as a lattice gas [20–24]. These lattice gas atoms give rise to weak diffuse intensity around the '$\sqrt{3}$' position in the LEED patterns as shown in Fig. 6.6 at $T = 896\,^{\circ}$C. We recorded LEED patterns of the clean Si(111) surface as a function of temperature in the range of about $T = 900\,^{\circ}$C to $T = 1150\,^{\circ}$C. The weak diffraction signal of the lattice gas is of the same order of magnitude as the encountered background due to inelastically scattered or secondary electrons. In a LEEM instrument, however, the inelastic background intensity is deflected off-center with respect to the elastically scattered intensity due to dispersion in the magnetic 90°-deflector that separates illuminating electrons and back-reflected electrons. Therefore, the weak diffraction signal of the lattice gas is detectable in the LEED pattern.

Figure 6.7 shows profile plots of the LEED pattern at five different temperatures taken through the center of two $\sqrt{3}$-spots and two adjacent integer spots (see

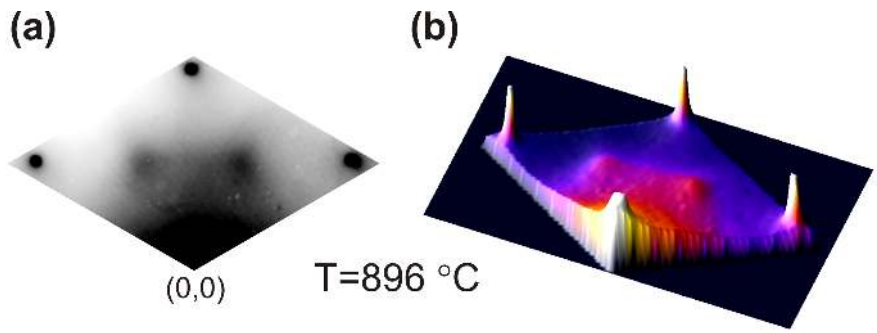

FIGURE 6.6: (a) LEED pattern of the Si(111) $-'(1\times1)'$ surface just above T_C at $T = 896°C$). (b) 3D intensity plot of the pattern in (a). Very weak but clear $\sqrt{3}$-spots are visible in the center surrounded by sharp integer spots.

dashed line in the inset in Fig. 6.7). The LEED patterns contain contributions from inelastically scattered electrons. That background intensity has been subtracted from the profile plots in Fig. 6.7 by subtracting a temperature-scaled background of the background extracted from a LEED pattern recorded just below T_C. The profile plots show relatively broad intensity peaks located at the $'\sqrt{3}'$-position. The intensity of these spots decreases rapidly with increasing sample temperature. Comparison with the profile plots from the SiC(0001)-$(\sqrt{3}\times\sqrt{3})$ (see inset in Fig. 6.7) shows that the width of the $\sqrt{3}$-spots is significantly larger in the Si(111) data. This clearly suggests that a lattice gas is formed on the Si(111) surface above T_C unlike the decaying but ordered $(\sqrt{3}\times\sqrt{3})$-adatom layer observed on SiC(0001) (see section 6.3.1).

Monte Carlo simulations of a lattice gas

It has been suggested earlier that the high temperature $'(1\times1)'$-structure consists of Si adatoms randomly occupying binding sites of a (1×1) substrate plane [20–24]. The (1×1) surface has one dangling bond per unit cell. It is, therefore, energetically favorable to have the (1×1) surface decorated with Si adatoms. Adatoms can sit on the threefold-hollow site (H_3) or the threefold-atop site (T_4) by forming covalent bonds with neighboring Si atoms of the underlying Si structure. The T_4-sites and the H_3-sites can be considered to form two separate triangular sublattices. In the case that two adatoms are so close that they would have to share one bond or more to the Si substrate they will repel each other. Therefore, such an adatom configuration is excluded and the adatom distribution is not completely random but does contain short-range order.

In principle, we can imagine adatom configurations where x% of the adatoms

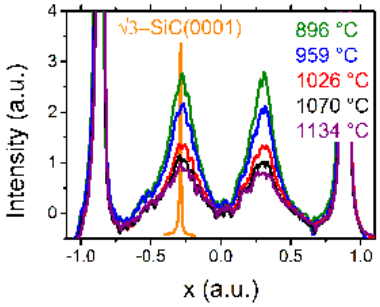

FIGURE 6.7: Profile plots taken through the center of two integer spots (far left and far right) and two $\sqrt{3}$-spots (broad spots in the center region) of LEED patterns of the Si(111) surface as a function of sample temperature. For comparison the $\sqrt{3}$-spot profile of a LEED pattern from the SiC(0001) is plotted to scale in width (orange curve). The width of the $\sqrt{3}$-spots is significantly larger compared to the $\sqrt{3}$-spots of SiC.

are located at T_4-sites and $(100-x)$% of the adatoms sit at H_3-sites with $x = [0,100]$. The total adatom concentration can be anywhere between 0% and 100%. It has been reported by Northrup [28], however, that a Si adatom on Si(111) sitting at a H_3-site is 0.64 eV per atom energetically less favorable compared to an adatom at a T_4-site. Hence, the probability of an occupied H_3-site is about 0.65% at 1200 °C assuming a Boltzmann distribution. Figure 6.9a shows LEED patterns obtained from MC simulations for different ratios of T_4/H_3 occupation at a fixed lattice gas density of $\rho = 0.2$ ML. We performed test calculations for T_4-site occupations of 90%, 95%, and 99% for different lattice gas densities, ρ, ranging from 0.17 ML to 0.25 ML. From these test calculations we know that a real space adatom configuration with 50% of the Si atoms located at T_4-sites and the remaining 50% sitting at H_3-sites yields LEED patterns with a very weak and very broad intensity distribution around (2×2)-spots without any clear indication of $\sqrt{3}$-spots (see black curve in Fig. 6.9a). Furthermore, a real space structure with 1% of the adatoms located at H_3-sites (close to the theoretically expected value of 0.65%) yields LEED patterns very similar to the ones obtained from real space adatom structures with all of the adatoms located at T_4-sites. Comparison of LEED patterns with a T_4-site ratio of 99% (see blue curve in Fig. 6.9a) and a T_4-site ratio of 100% (see red curve in Fig. 6.9a) shows that only a very minor difference in the intensity profile can be observed. Thus, we assume that we can neglect the effect of adatoms at H_3-sites on the LEED patterns for now. Below we will give a quantitative estimate of how the T_4/H_3-ratio changes the extracted lattice gas density. In the following, the MC simulations are performed with a T_4-site ratio of 100%.

The super cell used in the simulations contains 1000×1000 T_4-sites (see Fig. 6.8) with periodic boundary conditions. We start with defining the adatom density, ρ. Then, we randomly place adatoms at the T_4-sites of our simulation unit super-cell. This is done by randomly picking one of the 10^6 T_4-sites. An adatom is placed at a chosen T_4-site only if it is not already occupied and if all six direct neighboring T_4-sites are not occupied by adatoms (nearest-neighbor exclusion, see Fig. 6.8). Then, another random T_4-site is chosen. This is repeated until the specified adatom density is reached as long as the chosen density is below 1/3 ML. A perfect $(\sqrt{3}\times\sqrt{3})$-layer has a density of 1/3 ML referenced to the (1×1) structure. Therefore, the chosen lattice gas density needs to be always smaller than 1/3 ML otherwise there will not be enough T_4-sites with empty neighboring sites available. To further randomize the adatom structure we anneal the populated simulation super-cell. This is done by randomly choosing two T_4-sites of the cell. If one of the chosen sites is is occupied with an adatom and the other site is empty and if all direct neighboring T_4-sites of the empty site are also empty we move the adatom to the chosen empty T_4-site. This is repeated many times to assure a truly annealed real space adatom structure. For a good signal to noise ratio we need to have many of the annealed real space adlayer structures. We use the first real space structure (obtained as described above) as a starting point to form further uncorrelated real space adatom configurations by annealing. We average over 1000 uncorrelated real space structure units to calculate the LEED patterns shown in Fig. 6.9b.

We calculate the diffraction patterns of these simulated real space structures in the kinematic limit excluding multiple scattering events. Then, the diffracted intensity distribution is proportional to the lattice factor [29, 30]

$$I(\bar{k}) \propto \left| \sum_m e^{i\bar{k}\bar{r}_m} \right|^2 \tag{6.2}$$

with the scattering vector $\bar{k}$ and the contribution of m surface atoms at positions $\bar{r}_m$.

Figure 6.9b shows profile plots of the calculated diffraction patterns for different lattice gas densities. The intensity is normalized to the number of scatterers. We can see two very broad intensity maxima at the $\sqrt{3}$-positions with widths similar those encountered in the experimental data. In addition we see two integer spots at the far left and far right of the profiles. The intensity of the $\sqrt{3}$-spots clearly decreases with decreasing lattice gas density. Furthermore, a broadening of these spots takes places as the lattice gas becomes less dense as one can see by the upcoming tails of the $\sqrt{3}$-spots.

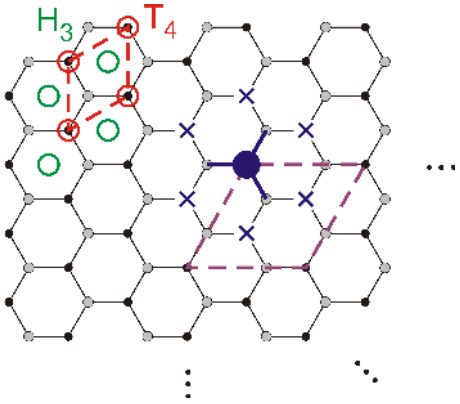

FIGURE 6.8: Schematic diagram of the real space structure of the Si(111) surface. Surface Si atoms are indicated by black (second surface layer) and gray (first surface layer) circles. The threefold-atop sites (T_4) are indicated in red and the threefold-hollow site (H_3) are indicated in green. In addition the (1 × 1) unit cell (dashed red lines) and the ($\sqrt{3} \times \sqrt{3}$) unit cell (dashed purple lines) are shown. A Si adatom (blue circle) placed on a T_4-site blocks all six nearest-neighboring T_4-sites (blue crosses).

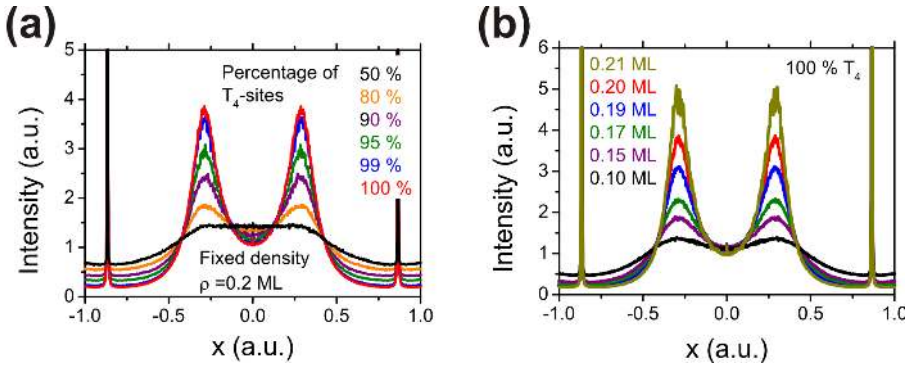

FIGURE 6.9: (a) Profile plots of calculated LEED patterns for a fixed lattice gas density of $\rho = 0.2$ ML with different percentage of H_3-site occupation in the range between 0% and 50%. (b) Calculated LEED pattern profiles for different lattice gas densities ranging from $\rho = 0.1$ ML to $\rho = 0.21$ ML with only allowing T_4-sites for adatoms.

Lattice gas density

Already by simple visual inspection we find that the calculated spot profiles resemble very well the overall shape and width of the spot profiles observed in the experiment. This gives us confidence that the chosen real space model for the adatom structure is indeed the real structure that gives rise to the experimental spot profiles. Next, the goal is to obtain quantitative information about the lattice gas density as a function of sample temperature. The experimental data gives us information about how the LEED spot profiles caused by the lattice gas depend on temperature. The data obtained from the Monte Carlo (MC) simulations tells us how the spot profiles change with changing adatom density. Therefore, by comparing the experimental data with the calculated spot profiles we are able to determine lattice gas density as a function of temperature.

First, we have to note that only the adatom layer is modeled in the MC simulations. Therefore, the integer LEED spots of the experimental data, which are caused mainly by the underlying bulklike Si(111) surface, are not reproduced accurately. The experimental integer spot profiles, however, can be well reproduced by a Lorentzian function of the form $L(x) = \frac{a\omega}{(x-c)^2+\omega^2}$ with amplitude a, peak position c, and width ω.

We compare the experimental data at each temperature with a series of calculated spot profiles for lattice gas densities ranging from $\rho = 0.1$ ML to $\rho = 0.25$ ML with steps of $\Delta\rho = 0.005$ ML. To quantify the agreement of the experimental data at a fixed temperature with each of the calculated profiles we define a cost function

$$\Delta\epsilon(\rho) = \min_{d,\beta,a,\omega} \left| f_{\mathrm{Exp}} - \left(d + \beta f_{\mathrm{Sim}}(\rho) + L_1 + L_2\right)\right| \tag{6.3}$$

with f_{Exp} the experimental data at a given temperature, f_{Sim} data of a calculated profile for a fixed lattice gas density and β a scaling factor. L_1 and L_2 are Lorentzians that resemble the integer spot profiles. They are located at fixed positions $c = \pm\frac{\sqrt{3}}{2}$ but have a variable width, ω, and a variable amplitude, a. The constant offset parameter d is to correct for a small but unknown offset in the experimental data due to inelastic scattering and thermionic emission. Therefore, we have four parameters to minimize our cost function. We find $\Delta\epsilon$ by first applying a global optimizer based on a simulated annealing algorithm and subsequently utilizing a local optimizer. We repeat this procedure to calculate $\Delta\epsilon$ for all the calculated profiles at different lattice gas densities for a fixed temperature. Figure 6.10a shows $\Delta\epsilon$ as a function of ρ for $T = 896\,^{\circ}\mathrm{C}$. The smallest value of $\Delta\epsilon$ corresponds to the best agreement between experimental data and one of the calculated profiles. Therefore, the clear minimum in Fig. 6.10a tells us that the Si(111) surface is covered with a lattice gas with a density $\rho = 0.21 \pm 0.01$ ML at $T = 896\,^{\circ}\mathrm{C}$. In Fig. 6.10b we plot the experimental data at $T = 896\,^{\circ}\mathrm{C}$ (red data points) and the

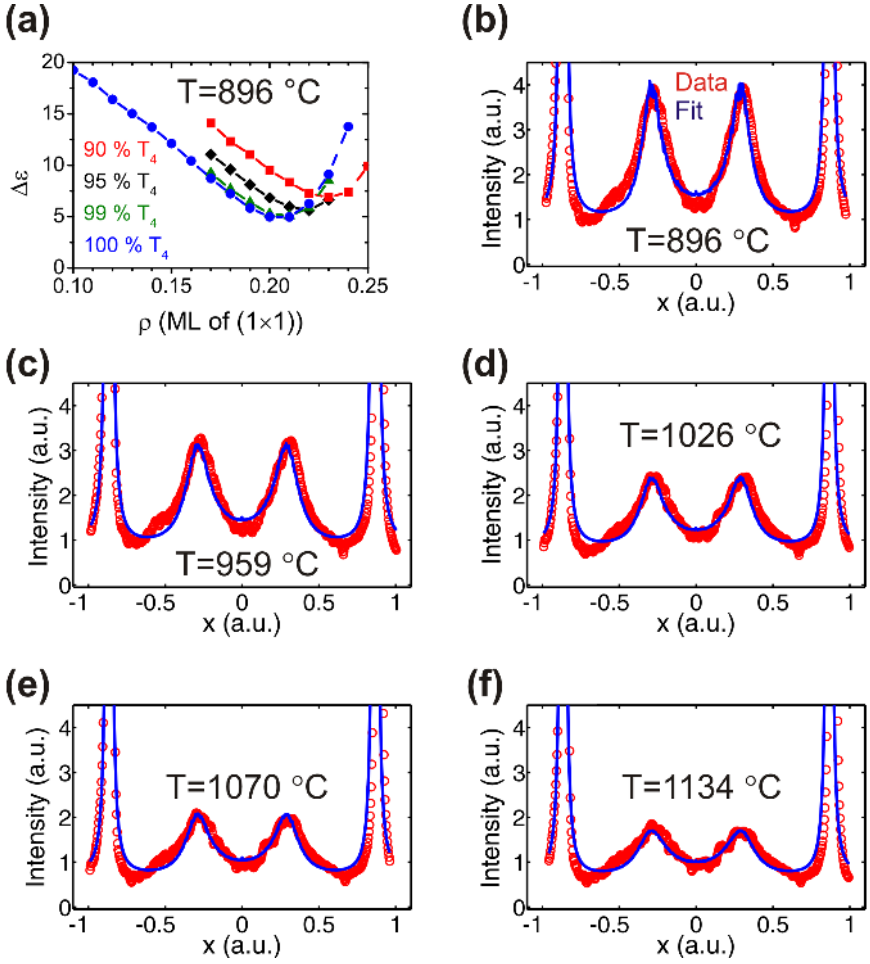

FIGURE 6.10: Comparison of the best fitting calculated LEED profiles with the experimental data at different temperatures. (a) Plot of $\Delta\epsilon$ as a function of calculated lattice gas densities for $T = 896\,^{\circ}\mathrm{C}$ for different T_4/H_3-ratios. For 100% T_4-sites the minimum of the blue curve gives the lattice gas density at $T = 896\,^{\circ}\mathrm{C}$. (b) Experimental LEED profile at $T = 896\,^{\circ}\mathrm{C}$ (red circles) and calculated LEED profile that best matches the experimental data (blue curve), i.e smallest $\Delta\epsilon$ equivalent to the minimum in (a). (c-f) Same as in (b) for different temperatures 959 °C, 1026 °C, 1070 °C, and 1134 °C.

best fit (blue curve), i.e. $s = d + \beta f_{\mathrm{Sim}}(\rho = 0.21) + L_1 + L_2$. The best fit reproduces the experimental data very well.

In the next step, we repeat the entire routine to calculate $\Delta\epsilon(\rho)$ for all the experimental data at five different temperatures. This yields the lattice gas density as a function of temperature. Figure 6.11 shows the lattice gas density as a function of temperature for two sets of experimental data. The density is nearly constant over the entire temperature range from about 900 °C to 1200 °C and has a value of $\rho = 0.20 \pm 0.01$ ML. This is in good agreement with previously reported results [20–24]. In particular Fukaya et al. [24] reported a constant lattice gas density of 0.25 ML in the temperature range 950 °C to 1160 °C as determined with reflection high-energy electron diffraction.

We can now determine the effect of the T_4/H_3-ratio on lattice gas density by using the calculated LEED profiles of different T_4/H_3-ratios and compare it with the experimental data using the above outlined approach. Figure 6.10a shows $\Delta\epsilon(T = 896\,^{\circ}\mathrm{C})$ as a function of lattice gas density for T_4-site ratios of 90% (red curve), 95% (black curve), 99% (green curve), and 100% (blue curve). The lattice gas density increases with increasing H_3-site occupation from 0.21 ML (100% and 99% T_4-sites) to 0.22 ML (95% T_4-sites) to 0.23 ML (90% T_4-sites). We can see in Fig. 6.10a that not only the lattice gas density increases but also $\Delta\epsilon$, i.e. the agreement with the experimental data, becomes worse as the occupation of H_3-sites increases. Thus, we find that the quality of the fits degrades when we introduce a significant number of H_3 adatoms, in agreement with theory. Based on these results, the adatom coverage can be given as $\rho = 0.20 + 0.03/-0.01$ ML in the temperature range of 900 °C to 1200 °C.

The intensity of the $\sqrt{3}$-spots clearly decays with increasing temperature (see e.g. Fig. 6.10b-f). However, no broadening of the spots takes places with increasing temperature as discussed above. The decreasing intensity can be explained by a Debye-Waller-factor which accounts for the increasing inelastic scattering with increasing temperature, a purely thermal effect. The elastically scattered intensity decreases exponentially with temperature

$$I = I_0 \exp(-W) \tag{6.4}$$

with I_0 the intensity at $T = 0$ K and the Debye-Waller-factor

$$W = \frac{\hbar^2 4\pi^2 \delta k^2}{m k_{\mathrm{B}} \Theta_{\mathrm{D}}^2} T. \tag{6.5}$$

Here, T is the sample temperature, Θ_{D} is the Debye temperature, m is the mass of the scattering center, $\hbar$ is the Planck constant, $\hbar(\Delta k)$ is the electron momentum transfer, k_{B} is the Boltzmann constant. The scaling factors β (see Eq.6.3) of the best

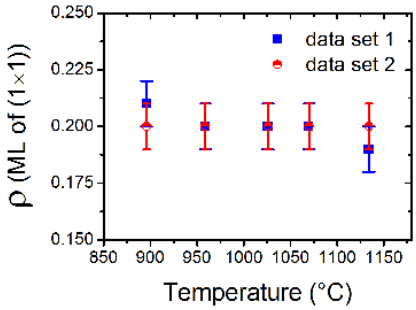

FIGURE 6.11: Lattice gas density on the Si(111) surface as a function of temperature. The error bars indication the uncertainty of the fit. $\rho = 0.2 + 0.03/-0.01$ ML independent of temperature in the range of about 900 °C to 1200 °C.

fits as function of temperature are a measure of the intensity decay with increasing temperature. Therefore, we can extract a surface Debye temperature of the lattice gas by fitting an exponential decaying function to $\beta(T)$. In our experiments we have $\Delta k = |k_{\text{out}} - k_{\text{in}}| = 53.14\text{nm}^{-1}$. We find a Debye temperature of $\Theta_D = 600 \pm 10$ K. This is close to the Debye temperature of bulk silicon $\Theta_D^{\text{bulk}} = 645$ K.

6.4 COMPARISON AND CONCLUSION

Our study of the Si(111) surface at elevated temperatures shows that the Si adatoms form a lattice gas with a density of $\rho = 0.20 + 0.03/-0.01$ ML. The lattice gas is in equilibrium with the step edges of the Si(111) surface. The lattice gas density is constant over the investigated temperature range from about 900 °C to 1200 °C. This is at first sight surprising since evaporation of Si from the surface takes place at the higher end of the temperature range. The step edges on the surface, however, can readily supply Si adatoms and the density stays constant even as temperature increases, indicating that the $'(1 \times 1)'$ adatom lattice gas is a thermodynamically stable phase over this temperature range.

On SiC(0001) a highly ordered $(\sqrt{3} \times \sqrt{3})$-layer of Si adatoms is formed. Again, with increasing temperature Si adatoms evaporate from the surface until equilibrium is reached with an external Si flux. The step edges on SiC cannot supply Si adatoms without also releasing C atoms onto the terraces. This happens only at higher temperature when the transition to the carbon-rich $(6\sqrt{3} \times 6\sqrt{3})$-phase takes place. With increasing temperature (but below the $6\sqrt{3}$ formation temperature), the fraction of the surface covered with $(\sqrt{3} \times \sqrt{3})$-domains decreases, as the $(\sqrt{3} \times \sqrt{3})$-layer breaks up in domains that shrink with increasing temperature, coexisting with the bare (1×1) structure. Just below the transition temperature to

the $(6\sqrt{3}\times 6\sqrt{3})$-phase the $\sqrt{3}$-domains vanish and the surface consists of just the bare (1×1) structure. The relatively sharp spot profiles of the $\sqrt{3}$-spots do indicate that it is energetically favorable on the SiC(0001) surface to form the coexisting $(\sqrt{3}\times\sqrt{3})+(1\times 1)$ phases rather than a lattice gas. On the SiC(0001) surface we find a temperature dependent coexistence of $(\sqrt{3}\times\sqrt{3})$ and (1×1) structures, unlike the adatom lattice gas found on Si(111).

Again, on the Si(111) surface the adatoms exist in equilibrium with the step edges which can provide an unlimited supply of adatoms. On the SiC(0001) surface, however, adatom supply from the step edges is accompanied by a simultaneous release of C atoms, and the formation of the $(6\sqrt{3}\times 6\sqrt{3})$ graphene structure. Thus, while the adatom phases on Si(111) and SiC(111) display many similarities, the atomic steps play very different roles on both surfaces.

Finally, we may ask if our results shed any light on the energetics of adatom structures on Si(111) and SiC(0001). It is well known that the Si and Ge (111) surfaces prefer to form local (2×2) structures [31, 32]. A (2×2) unit cell contains 4 surface atoms. Three of the surface atoms are capped by an adatom, with the T_4-site preferred over the H_3-site. There are now two three-fold coordinated atoms in the unit cell: the adatom and the so-called rest-atom. Without further modifications, both of these have a half-filled dangling bond orbital giving rise to a metallic surface state. However, on both Ge and Si there is an effective transfer of charge from adatom to rest-atom: the adatom now features an empty state orbital, and the rest-atom a lone-pair state. This electron transfer opens up an energy gap between these two states. The surface is no longer metallic, and the total energy is reduced. On Si(111) the (7×7) structure as well as the high temperature lattice gas structure consists of a mix of adatoms and restatoms, similar to the simple (2×2) structure. On SiC(0001) one might expect the same structural motif to be operational. Surprisingly, however, we find a $\sqrt{3}$ structure that is not observed for the clean Si(111) and Ge(111) surfaces. Experimentally, it has been established that T_4 adatoms decorate the SiC surface in a compact $(\sqrt{3}\times\sqrt{3})$ superstructure without restatoms [33, 34]. Each adatom then has a half-filled dangling bond orbital, and one would expect a metallic surface state. Energetically this is not very favorable. However, photoemission and STM experiments show that the surface is not metallic, but semiconducting. This is explained theoretically by strong electronic correlation effects giving rise to a Mott-Hubbard ground state with a large surface state bandgap [35]. Such strong correlation effects are absent for the Si and Ge surfaces. Thus, even at high temperature, when the $(\sqrt{3}\times\sqrt{3})$ structure is no longer stable against thermal evaporation of adatoms, co-existence of $(\sqrt{3}\times\sqrt{3})$ and (1×1) is energetically preferred over an adatom-restatom coexistence with a local (2×2) motif. While detailed calculations have been performed to assess both the electronic structure and the total energy of the SiC(0001) $(\sqrt{3}\times\sqrt{3})$ surface [36], no theoretical

comparison has been made with a (2×2) adatom-restatom structure. Therefore, we do not know theoretically if the same charge transfer mechanism that is operational on the Si and Ge surfaces could also occur on the SiC surface. With a much larger bulk bandgap and significantly lower dielectric constant, it is possible that such a mechanism is less favorable. Additionally, with the much smaller lattice constant of SiC (0.436 nm, vs. 0.543 nm for Si and 0.566 nm for Ge) the adatom binding may also be significantly stronger, leading to further stabilization of the $(\sqrt{3} \times \sqrt{3})$ structure. Our experiments indicate that the $(\sqrt{3} \times \sqrt{3})$ structure is more stable than an adatom-restatom lattice gas, indicating that a (local) (2×2) structure is energetically unfavorable. Further theoretical exploration of adatom energetics on SiC(0001) will be required to provide a definitive answer to these questions.

REFERENCES

[1] K. S. Novoselov, *Room-temperature quantum Hall effect in graphene*, Science **315**, 1379 (2007).

[2] K. S. Novoselov, *Two-dimensional gas of massless Dirac fermions in graphene*, Nature **438**, 197 (2005).

[3] K. S. Novoselov, *Unconventional quantum Hall effect and Berry/'s phase of 2[pi] in bilayer graphene*, Nature Phys. **2**, 177 (2006).

[4] Y. B. Zhang, Y. W. Tan, H. L. Stormer, and P. Kim, *Experimental observation of the quantum Hall effect and Berry/'s phase in graphene*, Nature **438**, 201 (2005).

[5] F. Schedin, *Detection of individual gas molecules adsorbed on graphene*, Nature Mater. **6**, 652 (2007).

[6] Y.-W. Son, M. L. Cohen, and S. G. Louie, *Half-metallic graphene nanoribbons*, Nature **444**, 347 (2006).

[7] B. Trauzettel, D. V. Bulaev, D. Loss, and G. Burkard, *Spin qubits in graphene quantum dots*, Nature Phys. **3**, 192 (2007).

[8] T. Yokoyama, *Controllable spin transport in ferromagnetic graphene junctions*, Phys. Rev. B **77**, 073413 (2008).

[9] C. Berger, *Ultrathin epitaxial graphite: 2D electron gas properties and a route toward graphene-based nanoelectronics*, J. Phys. Chem. B **108**, 19912 (2004).

[10] C. Berger, *Electronic confinement and coherence in patterned epitaxial graphene*, Science **312**, 1191 (2006).

[11] A. K. Geim and K. S. Novoselov, *The rise of graphene*, Nature Mater. **6**, 183 (2007).

[12] A. V. Bommel, J. Crombeen, and A. V. Tooren, *LEED and Auger electron observations of the SiC(0001) surface*, Surface Science **48**, 463 (1975), ISSN 0039-6028.

[13] R. M. Tromp and J. B. Hannon, *Thermodynamics and Kinetics of Graphene Growth on SiC(0001)*, Phys. Rev. Lett. **102**, 106104 (2009).

[14] J. B. Hannon and R. M. Tromp, *Pit formation during graphene synthesis on SiC(0001): In situ electron microscopy*, Phys. Rev. B **77**, 241404 (2008).

[15] K. Takayanagi, Y. Tanishiro, S. Takahashi, and M. Takahashi, *Structure analysis of Si(111)-7 × 7 reconstructed surface by transmission electron diffraction*, Surface Science **164**, 367 (1985), ISSN 0039-6028.

[16] J. Lander, *Chemisorption and ordered surface structures*, Surface Science **1**, 125 (1964), ISSN 0039-6028.

[17] S. Ino, *Some New Techniques in Reflection High Energy Electron Diffraction (RHEED) Application to Surface Structure Studies*, Japanese Journal of Applied Physics **16**, 891 (1977).

[18] P. Bennett and M. Webb, *The Si(111) 7 × 7 to '1 × 1' transition*, Surface Science **104**, 74 (1981), ISSN 0039-6028.

[19] N. Osakabe, Y. Tanishiro, K. Yagi, and G. Honjo, *Direct observation of the phase transition between the (7 × 7) and (1 × 1) structures of clean (111) silicon surfaces*, Surface Science **109**, 353 (1981), ISSN 0039-6028.

[20] H. Iwasaki, S. Hasegawa, M. Akizuki, S.-T. Li, S. Nakamura, and J. Kanamori, *Diffuse Scattering in the High-Temperature (1×1) State of Si(111)*, Journal of the Physical Society of Japan **56**, 3425 (1987).

[21] S. Kohmoto and A. Ichimiya, *Determination of the Si(111) '1 × 1' structure at high temperature by reflection high-energy electron diffraction*, Surface Science **223**, 400 (1989), ISSN 0039-6028.

[22] A. Latyshev, A. Krasilnikov, A. Aseev, L. Sokolov, and S. Stenin, *Reflection electron microscopy study of clean Si(111) surface reconstruction during the (7 x 7)-(1 x 1) phase transition*, Surface Science **254**, 90 (1991), ISSN 0039-6028.

[23] Y.-N. Yang and E. D. Williams, *High atom density in the '1×1' phase and origin of the metastable reconstructions on Si(111)*, Phys. Rev. Lett. **72**, 1862 (1994).

[24] Y. Fukaya and Y. Shigeta, *New Phase and Surface Melting of Si(111) at High Temperature above the (7 × 7) – (1 × 1) Phase Transition*, Phys. Rev. Lett. **85**, 5150 (2000).

[25] R. M. Tromp, M. Mankos, M. C. Reuter, A. W. Ellis, and M. Copel, *A New Low Energy Electron Microscope*, Surface Review and Letters **05**, 1189 (1998).

[26] J. B. Hannon, J. Tersoff, M. C. Reuter, and R. M. Tromp, *Influence of Supersaturation on Surface Structure*, Phys. Rev. Lett. **89**, 266103 (2002).

[27] S. G. Davis, D. F. Anthrop, and A. W. Searcy, *Vapor Pressure of Silicon and the Dissociation Pressure of Silicon Carbide*, The Journal of Chemical Physics **34**, 659 (1961).

[28] J. E. Northrup, *Origin of surface states on Si(111)(7×7)*, Phys. Rev. Lett. **57**, 154 (1986).

[29] M. A. Van Hove, W. H. Weinberg, and C. M. Chan, *Low-Energy Electron Diffraction: Experiment, Theory and Surface Structure Determination* (Springer, 1986).

[30] M. H.-v. Hoegen, *Growth of semiconductor layers studied by spot profile analysing low energy electron diffraction*, Zeitschrift für Kristallographie - Crystalline Materials **214**, 591 (1999), ISSN 2194-4946.

[31] J. E. Northrup and M. L. Cohen, *Total energy of the adatom and pyramidal-cluster models for Si(111)*, Phys. Rev. B **29**, 1966 (1984).

[32] R. D. Meade and D. Vanderbilt, *Adatoms on Si(111) and Ge(111) surfaces*, Phys. Rev. B **40**, 3905 (1989).

[33] A. Coati, M. Sauvage-Simkin, Y. Garreau, R. Pinchaux, T. Argunova, and K. Aid, *$(\sqrt{3}\times\sqrt{3})R30°$ reconstruction of the $6H-\mathrm{SiC}$ (0001) surface: A simple T4 Si adatom structure solved by grazing-incidence x-ray diffraction*, Phys. Rev. B **59**, 12224 (1999).

[34] L. Johansson, F. Owman, and P. Mårtensson, *Surface state on the SiC(0001)-$(\sqrt{3}\times\sqrt{3})$ surface*, Surface Science **360**, L478 (1996), ISSN 0039-6028.

[35] J. E. Northrup and J. Neugebauer, *Possibility of a Mott-Hubbard ground state for the SiC(0001) surface*, Phys. Rev. B **57**, R4230 (1998).

[36] J. E. Northrup and J. Neugebauer, *Theory of the adatom-induced reconstruction of the SiC(0001)$\sqrt{3}\times\sqrt{3}$ surface*, Phys. Rev. B **52**, R17001 (1995).